Reduced Graphene Oxide Nanosheets Decorated with Copper and Silver Nanoparticles for Achieving Superior Strength and Ductility in Titanium Composites

Longlong Dong [a, b], Wei Zhang [a], Yongqing Fu [c], Jinwen Lu [a], Xiaoteng Liu [c], Ning Tian [d, e], Yusheng Zhang [a, e*]

[a] Advanced Materials Research Central, Northwest Institute for Nonferrous Metal Research, Xi'an 710016, PR China

[b] School of Materials Science and Engineering, Northeastern University, Shengyang 110819, P.R. China

[c] Faculty of Engineering and Environment, Northumbria University, Newcastle upon Tyne NE1 8ST, UK

[d] School of Materials Science and Engineering, Xi'an Shiyou University, Xi'an 710065, PR China

[e] Xi'an Rare Metal Materials Institute Co., Ltd, Xi'an, 710016, PR China

Abstract: Graphene and its derivates are extensively applied to enhance the mechanical properties of metal matrix nanocomposites. However, their high reactivity with metal matrix such as titanium and thus the limited strengthening effects are major problems for achieving high-performance graphene-based nanocomposites.

* Corresponding author:
E-mail: y.sh.zhang@163.com, y.sh.zhang@c-nin.com (Y.S. Zhang)

Herein, reduced graphene oxide nanosheets decorated with copper or silver (i.e. Cu@rGO and Ag@rGO) nanopowders are introduced into Ti matrix composites (TiMCs) using multiple processes of one-step chemical co-reduction, hydrothermal synthesis, low energy ball milling, spark plasma sintering and hot rolling. The Cu@rGO/Ti and Ag@rGO/Ti nanocomposites exhibit significantly enhanced strength with superior elongation to fracture (846 MPa-11.6% and 900 MPa-8.4%, respectively, reaching the level of commercial Ti-6Al-4V titanium alloy), which are much higher than those of the sintered Ti (670 MPa-7.0%) and rGO/Ti composites (726 MPa-11.3%). Furthermore, fracture toughness values of the M@rGO/Ti nanocomposites are all significantly improved, i.e. the highest K_{IC} value is 34.4 $MPa \cdot m^{1/2}$ for 0.5Cu@rGO/Ti composites, which is 45.15% and 51.5% than those of monolithic Ti and 0.5rGO/Ti composites, respectively. The outstanding mechanical properties of Ag@rGO/Ti and Cu@rGO/Ti composites are attributed to effective load transfer of *in-situ* formed TiC nanoparticles, and formation of interfacial intermetallic compounds among the rGO nanosheets and Ti matrix. This study provides new insights and approach for fabrication of metal-modified graphene/Ti composites with a high performance.

Keywords: Titanium matrix composites, Mechanical properties, Reduced graphene oxides, Strength mechanism, Metal nanoparticles

1. INTRODUCTION

Recently, advanced metal matrix composites (e.g., Mg, Cu, Ti, Al based alloys) reinforced with nanoscale materials such as graphene nanoplates, reduced graphene oxides nanosheets and nano-TiB whisker have received considerable attention owing to their good mechanical properties, wear resistance and distinctive physical properties in comparisons to their monolithic counterparts. [1-6] On the other hand, titanium and its alloys with their high specific strength and good corrosion resistance are attractive for various industrial applications, including automotive, motorcycle, airplane, chemical and petrochemical industries. [7] Recent studies revealed that the properties of Ti materials can be further enhanced using graphene nanomaterials via optimal fabrication technologies and structural designs. [6, 8-10] However, the strengthening effects using graphene in the graphene/Ti system have often limited by easy agglomerations of graphene nanopowders in the matrix and weak interface bonding among graphene and Ti matrix, mainly due to large specific surface area and Van der Waals force of the graphene. [11-15] One of the viable approaches to simultaneously improving dispersion and wettability issues of graphene into metal matrix composites is to decorate it with suitable nanomaterials of metals or carbides. These metal/carbide nanoparticles/nanolayers decorated onto the surfaces of carbon nanomaterials (e.g., graphene, diamond and carbon nanotubes) can minimize the density differences between graphene and metal matrix, thus leading to improved dispersion effects of graphene. [16, 17] For example, Chu et al. fabricated graphene/Cu composites by adding Mo_2C nanoparticles onto graphene using spark plasma sintering (SPS) process and achieved 0.2% yield strength (0.2% YS) of 238 MPa, which is 58%

and 127% higher than those of the reduced graphene oxide/Cu and pure Cu. [18] Guan et al. prepared Ni-coated graphene nanosheets/Al matrix composites (with Ni contents of 0.5, 1.0, 1.5 and 2.0 wt%) using a vacuum sintering method followed by hot extrusion, and obtained 0.2% YS of 204.5 MPa and a maximum Vickers hardness of 65.3 $HV_{0.5}$. [19]

Although most studies demonstrate that graphene addition can enhance the mechanical properties on a certain degree, so far there are few studies using metallic nanoparticle decoration method for interfacial optimization and enhancement of the mechanical properties of graphene/Ti composites. The following issues are not well-understood: (a) what the possible interfacial microstructures between modified graphene and Ti matrix are; (b) what the strengthening mechanisms of the metal@graphene/Ti composites are; and (c) which metallic candidates shows the optimal strengthening effect in Ti matrix.

Herein, two types of metal nanoparticles (Cu and Ag) were decorated onto the reduced graphene oxides nanosheets (named as Cu@rGO and Ag@rGO for simplification) and then applied as reinforcements to fabricate metal coated rGO/Ti (e.g., M@rGO/Ti) composites. The M@rGO nanopowders were fabricated using a one-step chemical co-reduction process, [20, 21] and then incorporated into the Ti matrix to fabricated M@rGO/Ti composites using a powder metallurgy route. The influences of two types of M@rGO nanopowders on the interfacial microstructures and mechanical properties were investigated. In order to further verify the effects of M@rGO nanopowders on the strength and ductility of the Ti composites, various

concentrations of Ag@rGO nanopowders in the Ti composites were prepared and their mechanical properties were investigated. A special attention was paid on the understanding of effects of introduced metal nanoparticles on the interfacial structures and strengthening mechanisms of M@rGO/Ti nanocomposites.

2. RESULTS AND DISCUSSIONS

2.1 Microstructure and Composition of rGO/Ti and M@rGO/Ti Composite Powders

Scanning electron microscope (SEM) images of as-fabricated composites powders of M@rGO/Ti are shown in **Figure 1**. Compared with the pristine spherical Ti powders (**Figure S1a**), the sizes and shapes of the rGO/Ti and M@rGO/Ti powders in **Figures 1a** ~ **c** do not show apparent changes. This is mainly due to the lower energy and shorter time during ball milling process, which has little effect on the quality of rGO nanopowders and can be confirmed by Raman I_D/I_G values in **Figure S1b**. A small number of rGO clusters (denoted by the white arrow in **Figure 1a**) are clearly observed on the surfaces of Ti powders due to Van der Waals forces and large specific surface areas. [22] However, the surfaces of the M@rGO/Ti powders in **Figures 1b** and **c** are much rougher than those in **Figure 1a**, and without obvious agglomerations. Enlarged view images in **Figures 1b$_1$** and **1c$_1$** reveal that the metal nanoparticles are well-bonded with rGO nanosheets in the composite powders (X-ray diffractometry pattern shown in **Figure S1c**), suggesting a good bonding between Cu and Ag nanoparticles and rGO. Energy dispersive X-ray spectrum analyzer (EDS)

mapping analysis in **Figures 1b$_2$** and **c$_2$** show that the Cu@rGO and Ag@rGO nanopowders are distributed uniformly on the surfaces of Ti powders.

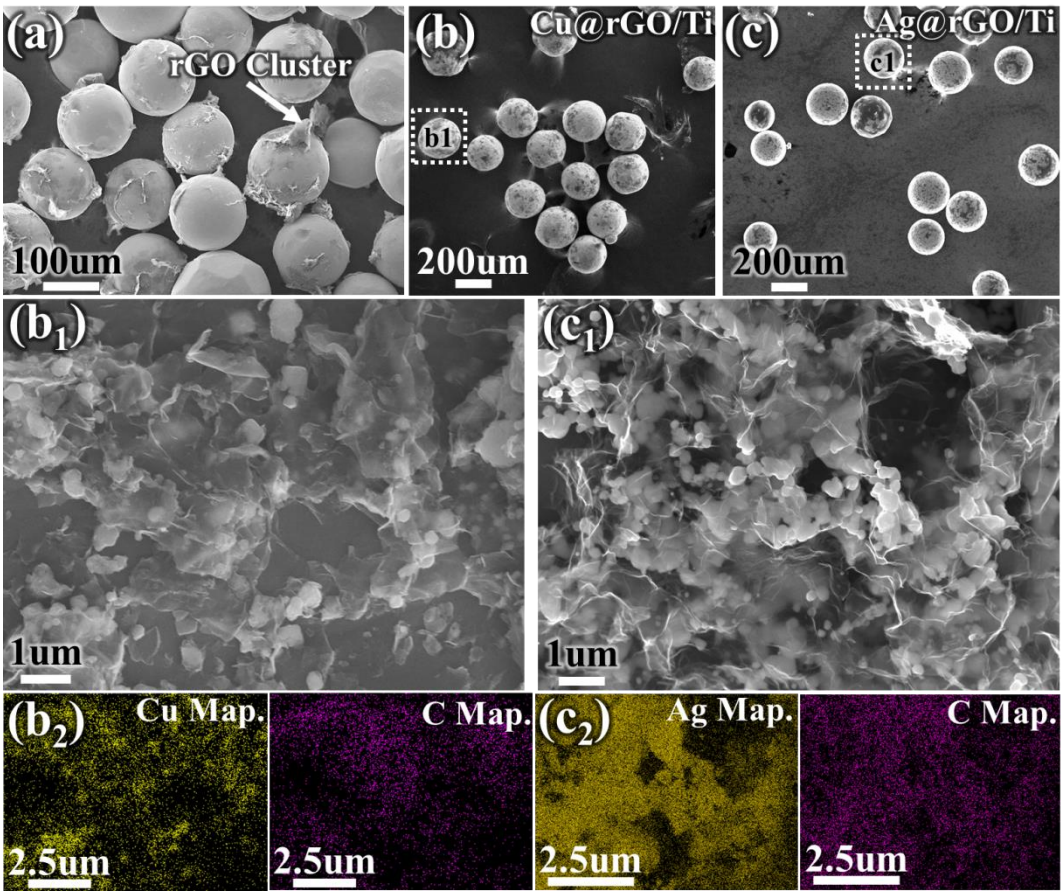

Figure 1. Characterization of as-received M@rGO/Ti composites powders by SEM. (a) 0.5rGO/Ti powders, (b) 0.5Cu@rGO/Ti powders, (c) 0.5Ag@rGO/Ti powders. (b_1) and (c_1) an enlarged view image of Cu@rGO and Ag@rGO nanopowders distribution on the surface of M@rGO/Ti composites powders recorded at the marked b_1 and c_1 in Figures b and c, respectively. (b_2) and (c_2) EDS elements distribution of Cu or Ag and carbon on the surface of 0.5Cu@rGO/Ti and 0.5Ag@rGO/Ti composites powders, respectively.

2.2 Interfacial Structure Analysis of the Composites

Figure 2 shows transmission electron microscope (TEM) images of 0.5rGO/Ti composites. As shown in **Figure 2a**, the wrinkled rGO nanosheets with various sizes are randomly dispersed on the boundaries of the Ti grains. The wrinkling and folding of rGO nanosheets provide effective mechanical interlocking with Ti matrix and restrict the plastic deformation of the composite.[23] The interfaces of TiC-rGO exhibit no apparent impurities, voids or gaps (**Figure 2b**). The interplanar distance of rGO in **Figure 2b** is measured as 0.342 nm, which is close to the theoretical inter-planar distance of C (0001).

Interfacial TiC nanostructures (denoted by white arrows in **Figure 2a**) are occasionally formed at rGO-Ti interface. This newly formed TiC phase can be identified by the high resolution TEM image with its corresponding Fast Fourier transform (FFT) and inverse Fast Fourier transform (IFFT) images, as shown in **Figures 2c**. The lattice parameter of TiC in **Figure 2c** is measured to be 0.2152 nm, corresponding to the interplanar spacing of TiC (200) plane. Based on the TiC-Ti interfacial analysis results shown in **Figures 2d** and **2e,** the *in-situ* TiC particles have a specific orientation with Ti matrix, formed during the *in-situ* growing process. Furthermore, the TiC-rGO interface was curvilinear with several side-steps (**Figure 2b**). The boundary between TiC and rGO is not clear and the crystallographic plane of the rGO side are clearly disordered (**Figure 2b**). However, the TiC-Ti interface in **Figures 2d** and **e** show clear and straight boundaries. It is commonly known that the presence of TiC phases at the interface shows a significant effect on the mechanical

properties of the composites. Lots of brittle TiC phases at the interface have a detrimental effect on the strength of the composites. However, formation of thin carbide layer or dispersed and distributed TiC nanoparticles are in favor of enhancing mechanical behavior via increasing the interfacial bonding. [24, 25, 26]

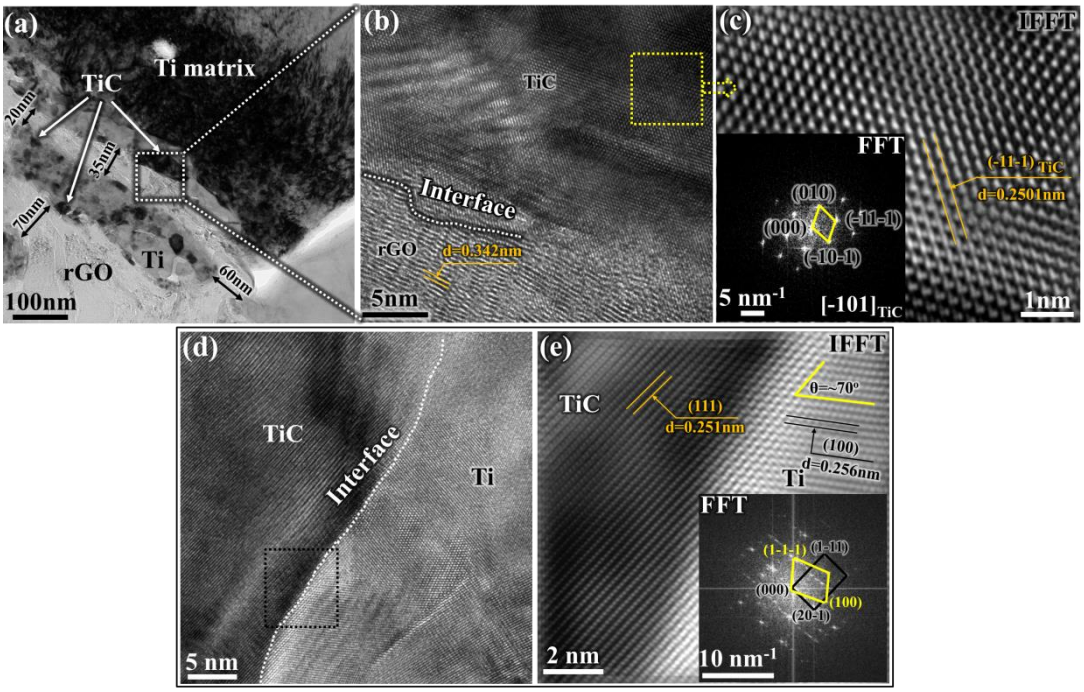

Figure 2. TEM analysis of rGO/Ti composites. (a) A bright field TEM image. (b) HRTEM image of TiC-rGO interface. (c) Inverse Fast Fourier transform (IFFT) image of TiC, inset shows the selected area electron diffraction (SAED) of TiC particles. (d) HRTEM image of TiC-Ti interface. (e) FFT and IFFT images of remarked region in Figure d, respectively.

Figure 3 presents the TEM images and their corresponding energy dispersive X-ray spectrometers (EDS) mapping analysis results of 0.5Ag@rGO/Ti composites.

As shown in the marked region in **Figure 3a,** the distinct and wrinkled phases are protruded from the Ti matrix, leaving behind the blurred interface but without the presence of visible voids or gaps. The chemical composition of the remarked region was then investigated using high-angle annular dark-field (HADDF) image (**Figure 3b)** with EDS mapping of C, Ag and Ti elements shown in **Figure 3c**. It can be clearly seen from **Figure 3c** that the Ag and Ti elements are enriched at the surface of rGO (i.e. C element), and some Ag and Ti are diffused into Ti matrix, resulting in an enhanced strength of the corresponding composites.

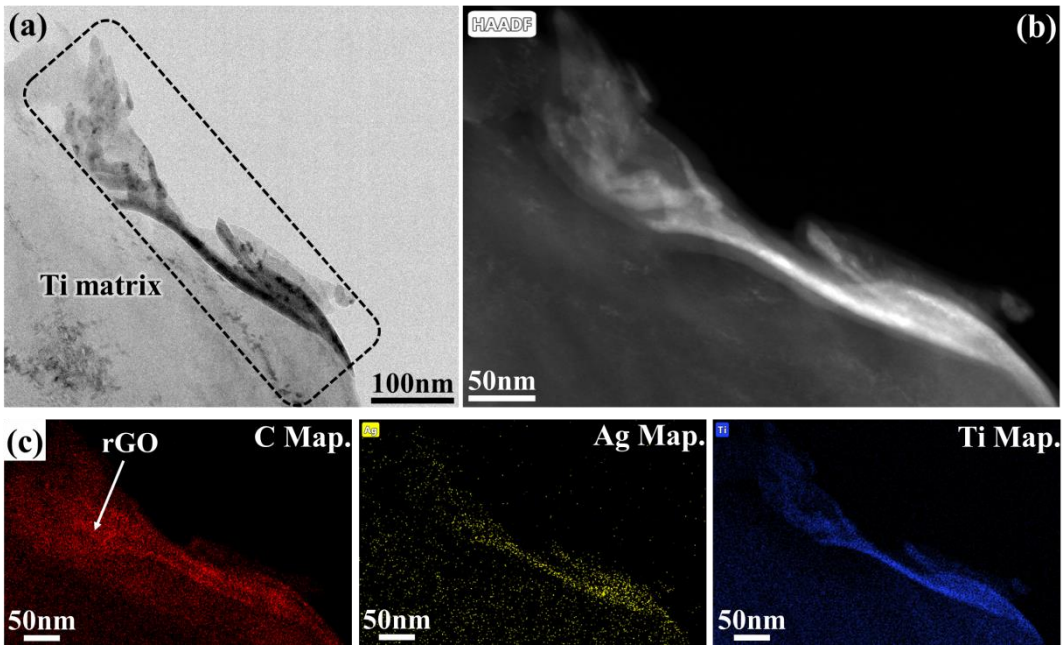

Figure 3. Typical TEM images taken from Ag@rGO/Ti composites. (a) A bright field TEM image. (b) High-angle annular dark-field-scanning transmission electron microscope (HADDF-STEM) image of the remarked region in Figure a. (c) Carbon, silver and titanium element distribution in Figure b, respectively.

Detailed TEM investigations on the interfacial structure of Ag@rGO/Ti composites are shown in **Figure 4**. It can be seen in **Figure 4a** that a crumpled and complex interface structure with a width of ~50 nm nanolayer was observed between the Ti grains. The marked region b in **Figure 4a** was analyzed in details using HRTEM, FFT and IFFT. The HRTEM image is shown in **Figure 4b**, which reveals that there are no visible interfacial voids or cracks near the interface, including three typical areas remarked with region b_1~b_3 (**Figure 4b**).

The HRTEM image shown in **Figure 4b** indicates the presence of ~5 nm thick interfacial transition nanolayer between the Ag@rGO and Ti matrix. The IFF diffraction pattern (**Figure 4b$_1$**) obtained from the marked region C exhibits (11-1), (1-11) and (200) diffraction patterns of Ti_3Ag along the [011] zone axis. The interfacial nanolayer is confirmed to be the Ti_3Ag, which is formed by the reaction of Ag nanoparticle (from the Ag@rGO nanoparticles) and Ti matrix. Ti_3Ag is a tetragonal structure with its space group of P4/mmm and unit cell parameters of a=0.4187 nm and c=0.3950 nm. [27] The IFFT image shown in **Figure 4b$_1$** reveals the lattice fringes with the measured inter-planar spacing of 0.207nm, closed to the plane of $(200)_{Ti3Ag}$. Yuan et al. demonstrated a similar Ti-Ag precipitated intermetallic in Ag-modified TiAl matrix composites. [28]

Ag@rGO nanolayer with a thickness of ~ 5 nm is observed in the 0.5Ag@rGO/Ti composites as shown in **Figure 4b**. The FFT pattern of the Ag@rGO region in **Figure 4b$_2$** shows the appearance of (0001) C and characteristic diffraction patterns of (002), (020) and (022) Ag plane, revealing that the Ag nanoparticles are

tightly attached on the surface of rGO nanosheets. These are beneficial for the enhancement of adhesive strength of Ag nanoparticles and rGO, and are in accordance with that obtained from the first principles analysis in our previous work. [18] We also found that TiC interfacial structures are formed between rGO and Ti matrix as shown in **Figure 4b** marked with b_3. The FFT and IFFT of TiC-Ti interface are shown in **Figure 4b$_3$** and the orientation relationships between *in-situ* formed TiC and Ti matrix are: $(111)_{TiC}//(100)_{Ti}$ & $[001]_{TiC}//[-101]_{Ti}$.

To compare Ti_xM_y nanolayers/nanoparticles in the M@rGO/Ti composites, the interfacial characteristics analysis of Cu@rGO/Ti composites was also performed, and the obtained results are shown in **Figure 5**. Apart from the Cu@rGO phases (**Figure 5a$_1$**) and *in-situ* formed TiC nanoparticles (**Figure 5a,** the interfacial characteristic of TiC-Ti shows in **Figures 5c**), the intermetallic Ti_2Cu phase can also be observed owing to the reaction of Cu and Ti during the SPS and hot rolling processes. The FFT and IFFT results shown in **Figure 5b$_1$** clearly reveal an orientation relationship of the Ti_2Cu and Ti along the $[-331]_{Ti2Cu}$ and $[100]_{\alpha\text{-}Ti}$ zone axes at the Ti_2Cu-Ti interface, which would provide an effective load transfer at the interface and the enhancement of strength from the nano-layer Ti_2Cu phase.

Compared with the rGO/Ti composites, the M@rGO applied into the Ti composites can: (1) improve the dispersion effect of rGO nanopowders in Ti composites (**Figure 1**) without formation of obvious clusters; (2) enhance the interfacial bonding between the rGO and Ti matrix; and (3) enhance effectively the load transfer at the interfaces between rGO-Ti owing to the formation intermetallic

M_xTi_y (like Ti_3Ag and Ti_2Cu) with high stiffness and strength (**Figure 4b** and **5b$_1$**).

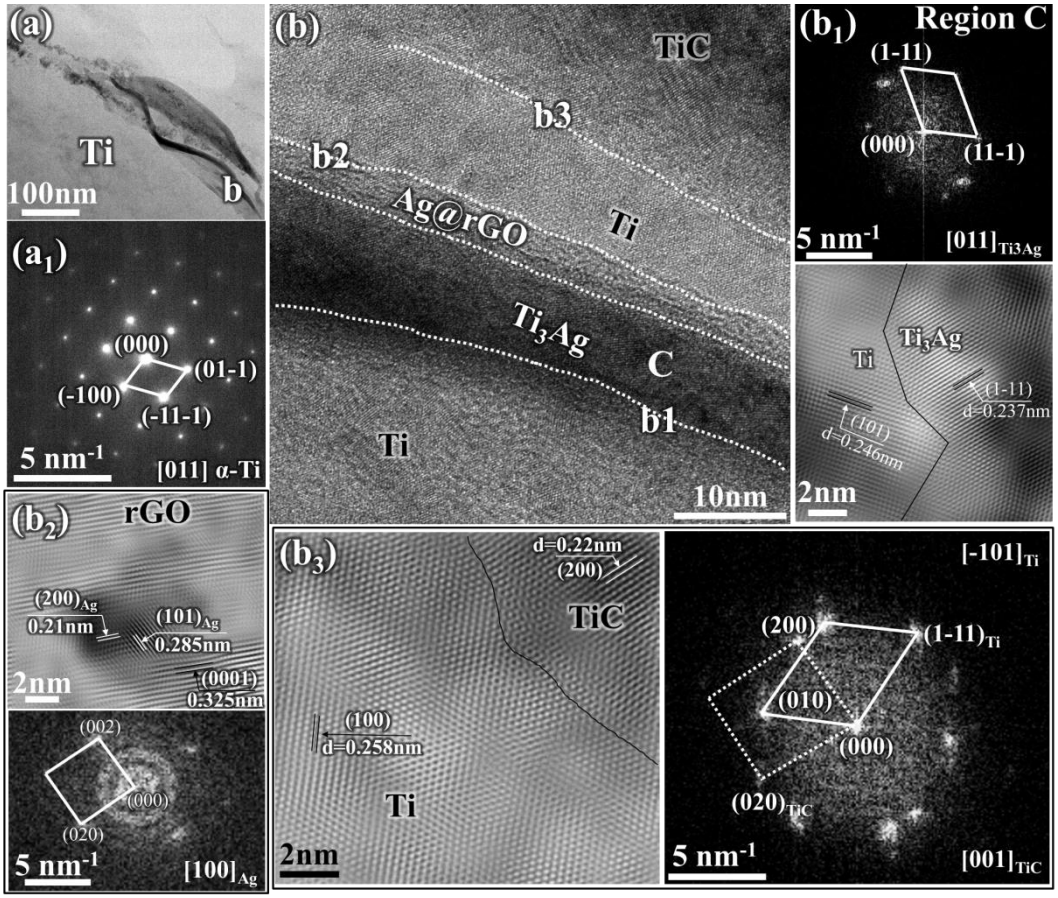

Figure 4. TEM observation and typical interfacial characteristics analysis on Ag@rGO/Ti composite. (a) Typical bright field TEM image. (b) High-magnification images of marked region in Figure (a). (b_1) Inverse Fast Fourier transform (IFFT) and SAED pattern of Ti-Ti_3Ag interface. (b_2) IFFT and SAED pattern of rGO-Ag interface, and a schematic illusion of the interface relationship between rGO and Ag. (b_3) IFFT and SAED pattern of TiC-Ti interface, respectively.

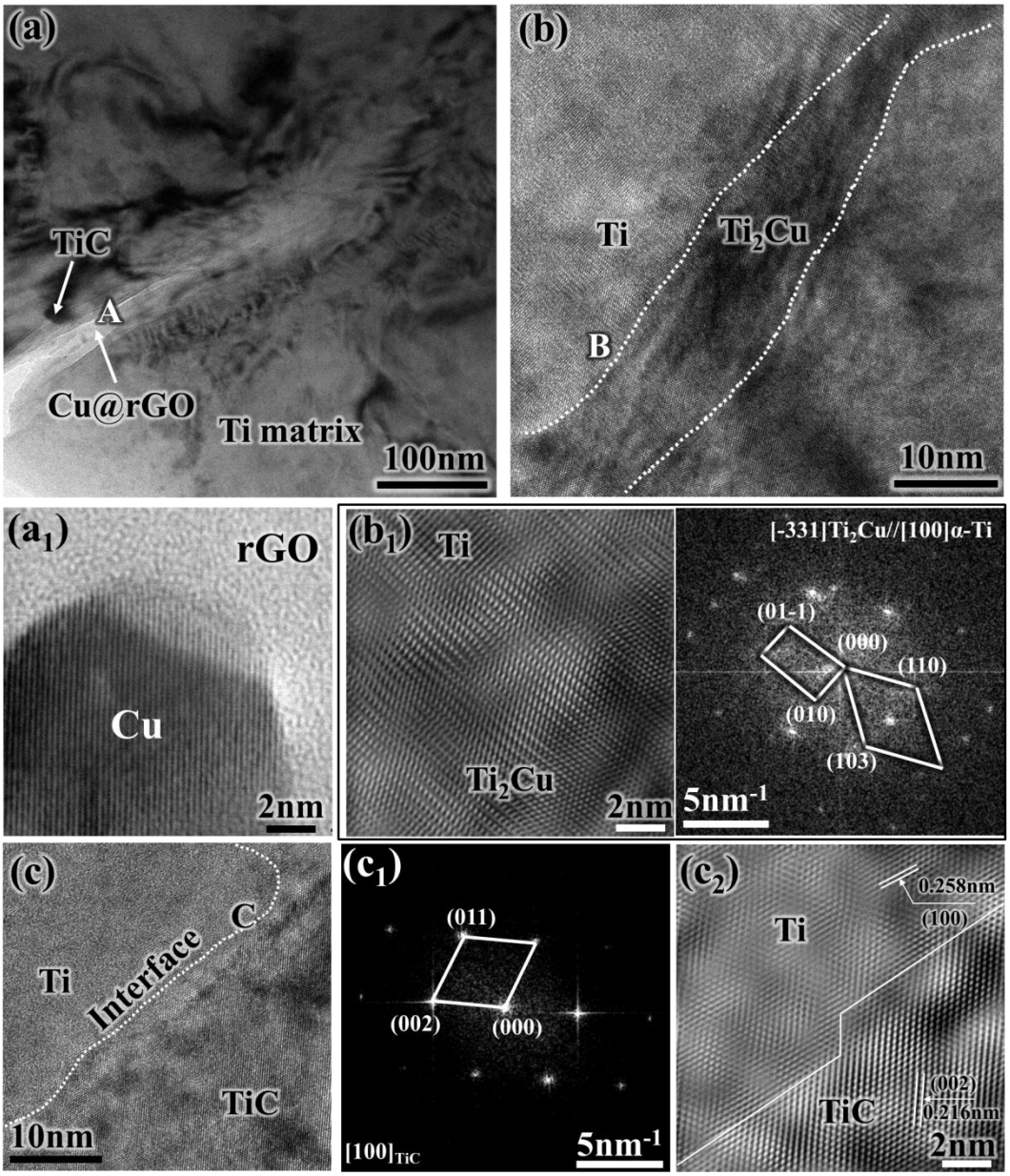

Figure 5. TEM observation and typical interfacial characteristics analysis on Cu@rGO/Ti composite. (a) Typical bright field TEM image. (a_1) HRTEM image of Cu@rGO in Figure a. (b) HRTEM image of marked A region in Figure a. (b_1) IFFT and SAED pattern of Ti-Ti_2Cu interface, respectively. (c~c_1) HRTEM, FFT and IFFT analysis of the Ti-TiC interface, respectively.

2.3 Mechanical Properties and Fracture Behavior

Figure 6a shows typical engineering stress-strain tensile curves of as-rolled composites, and the key mechanical properties obtained from the tensile tests are summarized in **Table 1**. Results show that the rGO nanosheets decorated with metal nanoparticles can significantly improve the mechanical properties of the Ti composites. Compared to those of the monolithic Ti matrix (0.2% offset yield strength, 0.2%YS=585 MPa, ultimate tensile strength, UTS=678 MPa), the 0.2%YS and UTS for 0.5Ag@rGO/Ti composites are 790 MPa and 900 MPa, which have been enhanced by 35% and 32.7%, respectively. The 0.2%YS and UTS values of the 0.5Ag@rGO/Ti composites are 28.5% and 25.7% higher than those of 0.5rGO/Ti composites (YS=615 MPa, UTS=716 MPa), while the elongation to fracture of 0.5Ag@rGO/Ti composites is still remained at 8.4%, revealing that the Ag nanoparticles/nanolayers contributes to the effective load transfer from Ti matrix to rGO nanosheets. The 0.2%YS and UTS of Ag@rGO/Ti composites are higher than those of Cu@rGO/Ti composites, which could be due to the grain refinement effect for the Ag@rGO/Ti composites. Furthermore, the composites with low volume fraction rGO contents exhibits a superior elongation, which can be attributed the four main reasons [29-32] : (1) the *in situ* reaction in the composites can improve the interfacial bonding between the reinforcement element and matrix; (2) the low volume fraction of rGO can be easily dispersed on the surface of Ti powders, which can generate a superior ductility and strain hardening effect; (3) the *in situ* hybrid reinforcements (rGO and TiC) are positive to the ductility of the composites; (4) the large size matrix region can withstand a large strain and result in a significantly

decreased speed of crack propagation.

The fracture surfaces of the Ti composites show a lot of dimples and cracks, which are mainly due to the significant differences in the deformation or mechanical properties between TiC and Ti matrix (**Figure S2**). [33] Compared with rGO/Ti composites (**Figure S2**), the M@rGO nanosheets were observed to be pulled out and fractured during the tensile deformation, revealing that M@rGO can absorb more energy and provide a better load transfer capability. [9]

Comparisons of the increased strength and ductility of TiMCs in the present work and those from literature are shown in **Figure 6b**. As can be seen, an inverse correlation can be clearly seen between strength and fracture to elongation for most of the reported TiMCs. Only a few TiMCs shows a good balance between strength and elongation, for examples, CNTs/Ti composites and the M@rGO/Ti composites in presented work. The M@rGO/Ti composites demonstrate both large strength and elongation than those of reported TiMCs. The main reason is attributed to the well-preserved rGO by surface metallization and the formation of *in-situ* TiC and Ti_xM_y nanoparticles/nanolayer at the interface, which can effectively balance the strength and ductility of graphene/Ti composites.

Figure 6c shows fracture toughness values of the as-rolled Ti composites at room temperature. Compared with that of monolithic Ti, the fracture toughness value (K_{IC}) of the 0.5rGO/Ti composite is decreased slightly. The lower K_{IC} values in 0.5rGO/Ti composites are linked to the presence of high contents of *in-situ* formed TiC particles which are easily broken under the compressive loading (**Figure S3b**)

and cause void formation. However, the K_{IC} values of the M@rGO/Ti composites are all significantly improved. The highest K_{IC} value is 34.4 MPa·$m^{1/2}$ for 0.5Cu@rGO/Ti composites, which is 45.15% and 51.5% than those of monolithic Ti and 0.5rGO/Ti composites, respectively. The volume fraction of TiC particles is relatively small in the M@rGO/Ti composites, because the metallic nanoparticles decorated on the surface of rGO nanosheets can significantly minimize the reactions between rGO and Ti matrix, thus the rGO nanosheets can prevent propagation of the crack's tip and provide an excellent load transfer capability. [33] Additionally, the dimple formation, quasi-cleavage fracture of the Ti grains, pull-out and micro-fracture of M@rGO nanosheets on the fracture surface of the M@rGO/Ti composites all absorb more energy during crack propagation (**Figures S3c** and **S3d**). As shown **Table 2** and **Figure 6b**, compared with other titanium composites reinforced with various reinforcements (like TiB, TiC, CNTs and Ti_5Si_3 etc.), the M@rGO/Ti composite in this study has a good combination of strength-ductility and toughness.

Table 1. Mechanical properties of rGO/Ti and M@rGO/Ti composites obtained in this work.

As-rolled composites	0.2% YS (MPa)	UTS (MPa)	FE (%)	Measured density (g/cm^3)	K_{IC} (MPa·$m^{1/2}$)
Pure Ti	580±5	670±8	7±1.2	4.484±0.006	23.7±2.3
0.2rGO/Ti	608±14	689±15	16±1.5	4.436±0.060	19.09±1.4
0.5rGO/Ti	625±10	726±13	11.3±1.4	4.487±0.011	22.7±1.7
0.5Cu@rGO/Ti	750±13	846±12	11.6±1.3	4.484±0.010	34.4±1.7
0.5Ag@rGO/Ti	790±9	900±15	8.4±1.4	4.479±0.013	26.6±1.9

* 0.2% YS= 0.2% Yield strength; UTS= Ultimate tensile strength; FE= Fracture to elongation

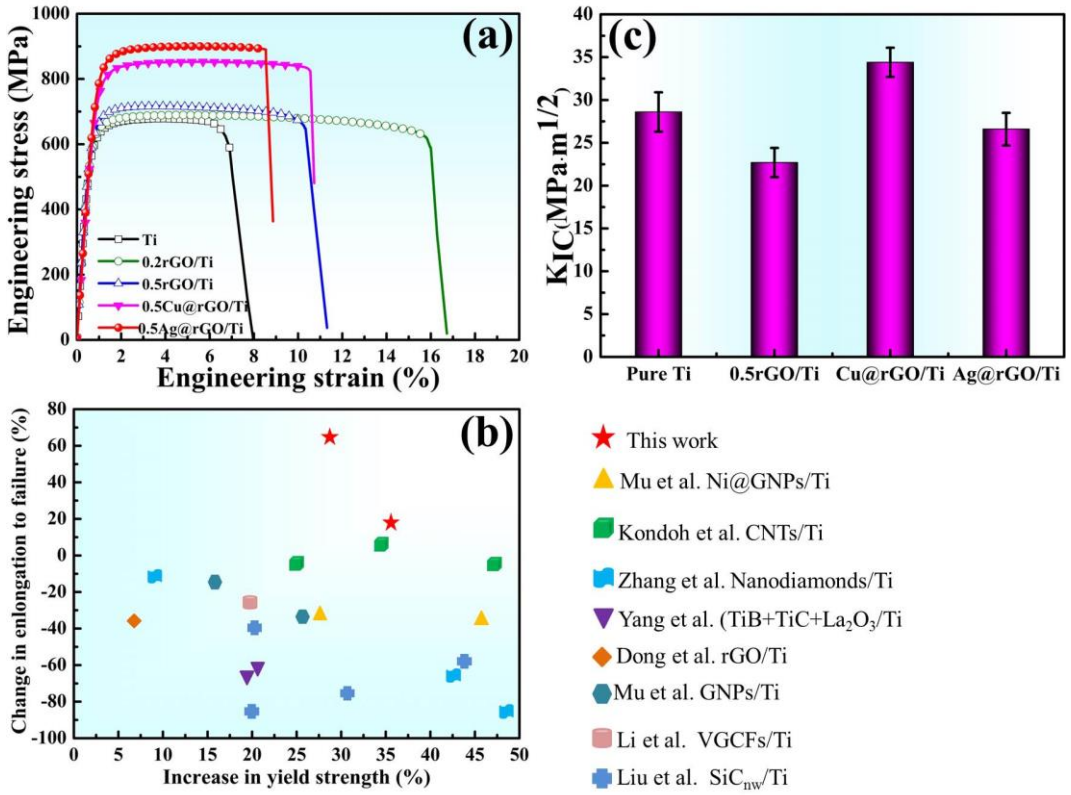

Figure 6. Mechanical properties of the as-rolled Ti and Ti composites in present work. (a) The representative engineering tensile stress-strain curves of as-rolled Ti composites. (b) Representative tensile properties of Ti composites in reported works. [34-41] (c) Fracture toughness of the composites.

To better understand the strengthening behavior of the rGO/Ti and M@rGO/Ti composites, *in-situ* tensile tests of 0.5Ag@rGO/Ti and 0.5rGO/Ti composites in **Figure 7** were performed inside the SEM chamber to real-time observe the fracture failure process of the composites. **Figure 7a** is the recorded load-displacement curve of rGO/Ti and Ag@rGO/Ti composites with several interrupted stages, revealing that the strength of Ag@rGO/Ti composites are higher than that of rGO/Ti composites. These results show same phenomena with the *ex-situ* tensile test shown in **Figure 6a**.

For the *in-situ* observation sample, a notch was pre-made on the tensile specimen to act as the stress concentration site (inset, **Figure 7a**), which is helpful to capture the crack initiation during the SEM observation. **Figure 7b** shows that a crack was generated in the pre-made notch area. Such the pre-crack will propagate in the following Stage ② and ultimately leading to fracture of the composite in Stage ③ with an increased tensile load. In Stage ③, the exposed Ag@rGO with a thickness of ~ 600 nm can be observed in the cracking area (**Figure 7c**), and it acts as a bridge to connect the fractured matrix (**Figure 7b**). However, no obvious rGO nanosheets are observed on the fracture surfaces of 0.5Ag@rGO/Ti composites after *in-situ* tensile test, except for the TiC particles and micro-void (**Figure 7d**). Pull-out phenomenon of 0.5Ag@rGO/Ti composites indicates the excellent load transfer from matrix to graphene, and this contributes to the enhance strength owing to the good interfacial bonding between graphene and Ti matrix in this work. This enhancement has also been reported in graphene or CNTs reinforced Cu, Al and Ti matrix composites. [24, 25, 51-53]

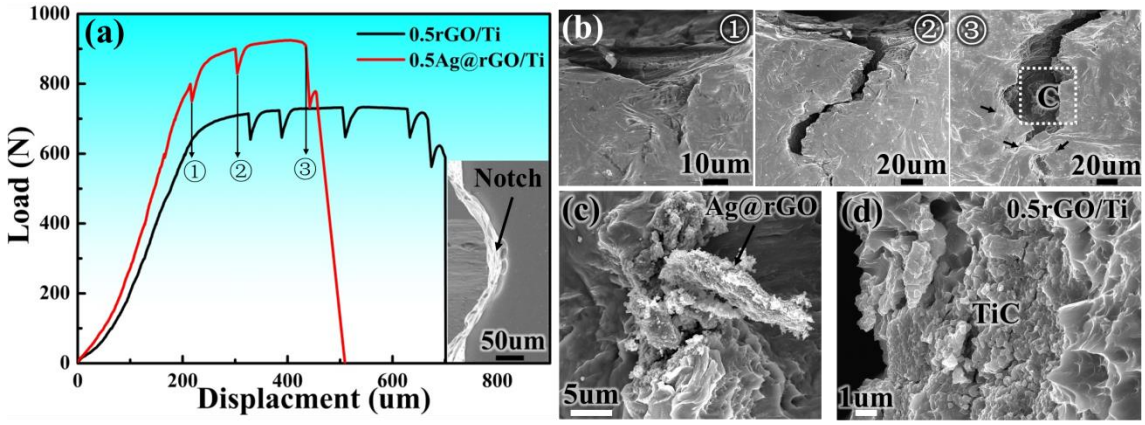

Figure 7. Failure behaviors of as-rolled rGO/Ti and Ag@rGO/Ti composites via

in-situ tensile tests. (a) Load-displacement curves of the composites with several paused stages, inset shows a notch is pre-made on tensile specimen before test. (b) Crack evolution and microstructure of rGO/Ti composites imaged at the paused stages ①~③ marked in (a). (c) An enlarged views of marked region C in Figure b for 0.5Ag@rGO/Ti composites, showing pulled-out Ag@rGO nanosheets. (d) Magnified image of the fractured surfaces of rGO/Ti composites, showing a mass of TiC particles located at the surface, respectively.

Table 2. Fracture toughness of graphene/Ti composites fabricated in presented work compared with other titanium composites reinforced with various reinforcements. [42-50]

Ti Matrix Composites	Fracture Toughness K_{IC} (MPa·m$^{1/2}$)	Preparation Technology	Reference
TiB/Ti	13.9		42
TiB/Ti-4Fe-7.3Mo	9.6	SPS	43
TiB/Ti	9.3		44
TiB/Ti-5.2Fe-7.8Mo-1.8Al	23	Electric field assisted sintering	45
CNTs/Ti-6Al-3.5Sn-9Zr-0.5Mo-0.4Si-0.7Nb	22	Vacuum consumable Smelting+forging	46
(TiB_w+TiC_p)/Ti-3.5Al-5Mo-6V-3Cr-2Sn-0.5Fe	45.5	Vacuum consumable Smelting+solution	47
TiC/Ti	16.48	Vacuum hot-pressing	48
(TiC+Ti_5Si_3)/Ti-6Al-4V	9.9	High-energy electron-beam irradiation	49
TiB/Ti-Fe-Mo	14.5/14.22/12.91	SPS/Hot Isostatic Pressing/Vacuum Sintering	50
Cu@rGO/Ti	34.4	SPS+Hot rolling	This work
Ag@rGO/Ti	26.6		

2.4 Strengthening Effect of M@rGO/Ti Composites

Excellent interfacial bonding between the nanoscale rGO reinforcements and Ti matrix play a significant role in guaranteeing the strengthening effect in the nanocomposites. Generally, the following strengthening mechanisms are reported in graphene/metal matrix composites, e.g.,: (1) solution strengthening; (2) grain refinement strengthening; (3) thermal mismatch strengthening; (4) strengthening of *in-situ* formed carbide or intermetallic nanoparticles/nanolayers; and (5) load transfer. To investigate the quantitative contribution of different strengthening effects of M@rGO nanoparticles, the as-rolled 0.5Ag@rGO/Ti composites were chosen.

In this work, considering that thermal mismatch strengthening can only take effect in a rapid cooling condition, such as quenching, it can be negligible because only the air-cooling procedure was used after hot rolling process. [24, 25]

The strength and hardness of Ti alloy materials can be improved by doping with oxygen and nitrogen elements according to their interstitial solution into α-Ti, whereas such effect should be ignored due to the short-time ball milling and rapid sintering process. However, interstitial solution strengthening of carbon atom should be considered owing to the high contents of carbon content (i.e., graphene) in the composites. However, further additions of carbon above its limit (~0.05 wt% for α-Ti at room temperature) have little contribution to the enhancement of strength. Munir et al. reported that solid solution strengthening ($\Delta\delta_{SS}$) by carbon interstitial atoms contributes up to 7 MPa per 0.01 wt% carbon. [54] Based on this estimation, the $\Delta\delta_{SS}$ contribution in 0.2% YS of graphene/Ti composites by carbon additions can be

estimated as 35 MPa for all the composites.

Grain refinement effect generally shows an important contribution on enhancement in strength in the graphene/metal composites. [55, 56] Generally, grains/sizes of particles increase at a higher operating temperature and longer holding time. However, for the M@rGO/Ti composites, M@rGO nanopowders are mostly surrounded with the Ti matrix (**Figures 1b ~ c**), restricting their significant grain coarsening during the SPS and rolling. Furthermore, the rapid SPS process was adopted to densify the mixed powders. As a result, the Ti grain size is obviously refined. Specially, the grain size in M@rGO/Ti composites is much smaller than those in Ti matrix and rGO/Ti composites (**Figure S4**). The strengthening contribution by grain refinement ($\Delta\delta_{GR}$) can be calculated through the Hall-Petch relationship [35]:

$$\Delta\delta_{GR} = k(d_C^{-0.5} - d_M^{-0.5}) \quad (1)$$

where k is a constant of 0.68 MPa $m^{1/2}$ for pure Ti , [35] d_M and d_C are the average grain size of Ti matrix and composites, respectively.

For the graphene/metal composites, it is generally accepted that the efficient load transfer from the graphene to Ti matrix is the most important strengthening mechanism due to the high aspect ratio and large specific surface area of graphene. [57] The high load transfer efficiency of graphene/Ti composite is evidenced by the strong interfacial bonding. In addition, Orowan strengthening takes effect for the composites with nanosized particles uniformly dispersed within the grains of the matrix. In such case, the adjacent intragranular nanoparticles can accumulate, pin down and form dislocation loops, which generate a remarkable back-stress that blocks dislocation

propagation across the nanoparticles and strengthens the metal matrix. However, TEM image in **Figure 2** and HRTEM image in **Figure 3** shows that *in-situ* formed TiC and Ti_3Ag intermetallic compound nanolayer as well as remained rGO nanosheets are always located at the grain boundaries of titanium. Furthermore, superior interface adhesion can be achieved without any micoviods at Ti-TiC, Ti_3Ag-Ti and Ag@rGO-Ti interfaces as shown in **Figure 4b**. Hence, as also reported in previous studies, [16, 58, 59] we hypothesize the load transfer produced by the *in-situ* formed TiC, Ti_3Ag and Ag@rGO nanosheets is the another strengthening mechanisms. Theoretically, the strengthening contribution by load transfer in composites ($\Delta\delta_{LTS}$) can be simply interpreted by the shear lag model as: [54]

$$\Delta\delta_{LTS} = \Delta\delta_{LTS-TiC} + \Delta\delta_{LTS-Ti3Ag} + \Delta\delta_{LTS-rGO/Ag} \quad (2)$$

$$\Delta\delta_{LTS} = \Delta\delta_{M}[\frac{f_{VR}(S+4)}{4} + f_{VM} - 1] \quad (3)$$

where δ_M is the 0.2%YS of Ti matrix, S is the width-to-thickness ratio of the reinforcements, f_{VM} and f_{VR} are the volume fractions of the matrix and reinforcements, respectively. The value of $\Delta\sigma_{LT}$ is proportional to the f_{VR} and S. However, the volume fraction of intact rGO, and *in-situ* formed TiC and Ti_xM_y phases cannot be calculated accurately for the composites after hot rolling. Although it is difficult to calculate the increase in the 0.2%YS contributed by the load transferring effect from Eq. (4), the strengthening contribution can be the sum of the above three strengthening factors, which can be expressed as:

$$\delta_{YC} = \Delta\delta_{GR} + \Delta\delta_{LTS} + \delta_{SS} + \delta_{M} \quad (4)$$

where δ_M is the 0.2%YS of the matrix. Hence, the load transfer strengthening of

M@rGO/Ti and rGO/Ti composites ($\Delta\delta_{LTS}$) can then be estimated using: $\Delta\delta_{LTS} = \delta_{YC} - \delta_{SS} - \Delta\delta_{GR} - \delta_{M}$. The obtained strengthening factors contributions to the increased strength of the 0.5Ag@rGO/Ti, 0.5Cu@rGO/Ti and 0.5rGO/Ti composites are summarized in **Figure 8a**. We can observe that the load transfer presents the major role for strengthening mechanism in Cu@rGO/Ti and Ag@rGO/Ti composites, and then followed by refinement strengthening. However, the refinement effects in the Ag@rGO/Ti composites are more significant than that in the Cu@rGO/Ti composites. Though Ag and Cu have similar characteristics of "eutectoid stabilizer elements" in Ti alloy materials, Cu possesses a faster diffusion effects than Ag in α-Ti. [60] Hence, more Cu atoms could diffuse into Ti's intragranular positions to form Ti_xCu_y alloys during SPS and HR. On the contrary, most of the Ag@rGO are still remained at the grain boundary, impeding movement of the grain boundaries.

Based on **Figure 8a,** $\Delta\delta_{LTS}$ values of M@rGO/Ti composites are significantly higher than that of rGO/Ti composites, revealing the superior load-baring capability of combination of TiC, Ti_xM_y and M@rGO in M@rGO/Ti composites. The poor $\Delta\delta_{LTS}$ values in the rGO/Ti composites are attributed to the agglomeration of rGO and higher contents of formed TiC. These findings emphasize the unique role of metal nanoparticles or nanolayers in enhancing the strength of Ti matrix composites.

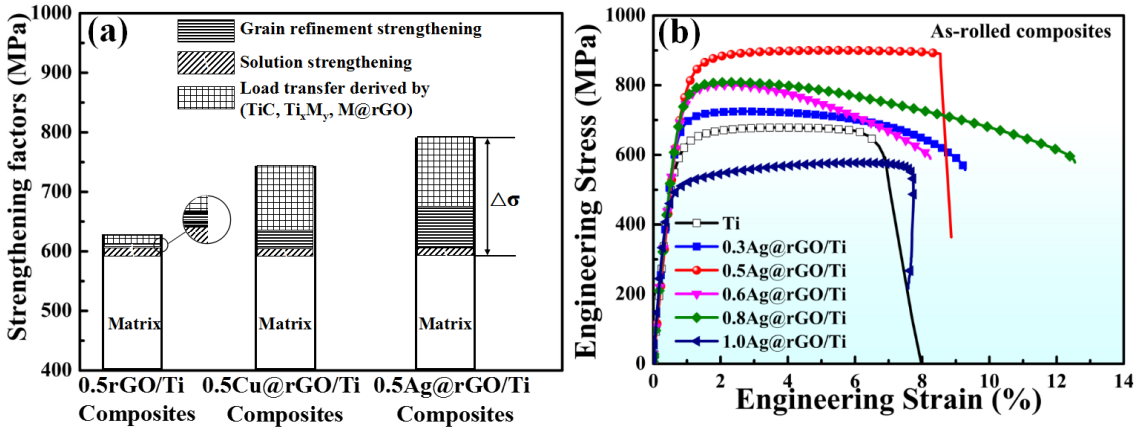

Figure 8. (a) Strengthening contributions of each factors to the as-rolled Ti composites in this work. (b) Mechanical properties of Ti composites with various Ag@rGO contents.

In order further to verify the strengthening effects of M@rGO nanopowders on the strength and ductility of the Ti composites, we have investigated the influence of concentrations of Ag@rGO nanopowders on the mechanical properties of Ti composites using the same method we have proposed (**Section 4**). The obtained tensile testing results of the *x*Ag@rGO/Ti composites (x=0.3, 0.5, 0.6, 0.8 and 1.0wt %) shown in **Figure 8b** reveal that the 0.5Ag@rGO/Ti composites exhibit the highest strength and good ductility, whereas the composites with a lower Ag@rGO content (0.3 wt%) and a higher Ag@rGO content (1.0 wt%) show the reduced strength of the composites, which is mainly due to the large contents of interfacial products Ti_3Ag and TiC. In fact, excess of Ti_xM_y phases can make the interface of Ti-Ti_xM_y quite brittle, whereas inadequate Ti_xM_y cannot provide adequate interfacial bonding and efficient load transfer.

3. CONCLUSIONS

In summary, we provide a novel strategy for obtaining high-performance graphene/Ti composites using SPS and hot rolling process via introduction Cu@rGO and Ag@rGO nanopowders into Ti matrix. The balance of enhanced yield strength and good elongation to fracture is achieved in the Ag@rGO/Ti and Cu@rGO/Ti composites. The UTS, 0.2%YS and fracture toughness of 0.5Ag@rGO/Ti composites are 900 MPa, 790 MPa and 26.6 MPa·$m^{1/2}$, which are 32.7%, 35.04% and 12.23% increments, compared with those of the monolithic Ti. *In-situ* formed TiC, nano-scale Ti_xM_y interface and M@rGO nanophase play critical roles in the strengthening behavior of M@rGO/Ti composites. Load transfer effects due to these nanophases (i.e. TiC, Ti_xM_y and M@rGO) and refinement strengthening are major strengthening mechanisms of the M@rGO/Ti composite. However, load transfer strengthening has less significant role in the strengthening of rGO/Ti composite owing to the poor distribution effect of rGO and interfacial bonding. These findings reveal that metal nanoparticle (such as Cu or Ag) modified graphene nanomaterials is a promising reinforcement for the design and fabrication of advanced graphene/Ti composites.

4. EXPERIMENTAL SECTION

4.1 Preparation of M@rGO/Ti Composites

Preparation procedures of graphene oxides (GO) nanosheets using the Hummers method have been described elsewhere, [61] which were purchased from XFNANO Technology Co., Ltd., China. As-synthesized GO nanosheets were reduced into the

reduced graphene oxides and simultaneously coated with metal nanoparticles (i.e. M@rGO=Ag@rGO and Cu@rGO) using one-step chemical co-reduction route (**Figure S5**). [20, 21] All the chemicals were used directly without further purification. Spherical Ti powders were purchased from Xi'an Sino-Euro Materials Technologies Co., Ltd., China. The copper and silver were chosen as metallization alloying elements to modify reduced graphene oxide nanopowders because they show optimal growth relationships on surface of graphene nanomaterials, [62-64] especially because they are all eutectoid elements in Ti alloy materials. The Ti alloys with appropriate copper or silver concentrations were reported to show good biocompatibility, corrosion resistance, tribological properties and mechanical properties. [65-67] For example, a solid solution treatment of the Ti-3Cu alloy can increase the 0.2% YS from 400 to 740 MPa and improved the antibacterial rate from 33% to 65.2%, which was demonstrated that homogeneous distribution and fine Ti_2Cu phase plays an important role in mechanical properties, corrosion resistance and antibacterial properties . [68]

In order to disperse uniformly the M@rGO nanopowders in the Ti matrix, M@rGO nanopowders and pure Ti powders were continuously stirred with the help of the ultrasonic vibration until a semi-solid state was obtained, and then the mixed powders were subjected to a low energy ball milling using a planetary mixing machine (QM-3SP4) for 30 min at a speed of 200 r/min with the ball-to-powder ratio of 6:1. The mixed M@rGO/Ti powders were sintered at 900 ^{o}C for 5 min under a pressure of 60 MPa using the SPS (SPS-80T-20). For comparisons, the unreinforced Ti materials were also fabricated using the same SPS process by direct consolidation

of spherical Ti powders. The rGO/Ti composites were also synthesized via the same mixture process and SPS process as M@rGO/Ti composites. Finally, all the samples were hot-rolled at 1000 ºC with a 83.3% reduction in thickness and the final thickness is about 1 mm.

4.2 Microstructure Characterization

The rGO and M@rGO nanopowder distributions on the surfaces of composites powders were observed using a field scanning electron microscope (FE-SEM, Zeiss GeminiSEM 500). The phase composition and structure of the composites were observed using X-ray diffractometry (XRD). The interfacial characteristics of the composites were observed using transmission electron microscope (TEM, FEI Talos F200X) and high resolution TEM (HRTEM). The TEM samples were prepared using a focused ion beam (FIB) system (Tescan LYRA3) finishing with a sample thickness of ~100 nm. Electron backscattered diffraction (EBSD) technique was used to obtain the grain size of as-rolled composites. The EBSD analysis area was 450 μm×340 μm with a step size of 1.2 μm.

Raman spectroscopy was used to investigate defects in the M@rGO, and the scan range of laser beam was from 1000 to 2200 cm^{-1}. The tests were performed at room temperature using a Laser Raman Spectrometer (LabRAM HR Ecolution) with an excitation wavelength of 532 nm.

4.3 Mechanical Properties of the Composites

The density of fabricated composites was measured using the Archimedes' principle. As listed in **Table 1**, the measured densities of all samples are closed to the

theoretical density of Ti with a value of 4.51 g/cm^3, revealing that all of composites possess a high relative density. Fracture toughness and room temperature tensile test were carried out to evaluate the mechanical properties of the as-rolled Ti composites. The fracture toughness of the as-rolled composites was obtained using a universal testing system with a crosshead speed of 0.5 mm/min. The fracture toughness values were calculated by analyzing the load–displacement curves, according to ASTM E399 with the following formula: [69]

$$K_{IC} = \left(\frac{P_Q S}{B W^{3/2}} \right) f\left(\frac{a}{W} \right) \quad (5)$$

where P_Q is the conditional load, KN; S is the span between two pivot points when testing (30 mm); B is the thickness (1 mm); W is the width (4 mm); a is the initial crack length (2 mm) and $f(a/W)$ is the geometry factor. The schematic drawing of the compact-tension specimen for fracture toughness test is illustrated in **Figure S6a**.

The *ex-situ* room temperature tensile test was conducted on an UTM5105X universal machine with a speed of 1 mm/min. The tensile axis of the tensile tests was parallel to the rolling direction. The final strength and ductility values were measured from three samples. The test samples were designed to be with a gauge length of 50 mm and section of 1 mm×13 mm (**Figure S6b**). Additionally, in order to investigate the fracture failure process and strengthening mechanism of Ti composites, an *in-situ* tensile test was performed via operating the tensile stage with Ti composites sample inside the an SEM (FE-SEM, Zeiss GeminiSEM 500) chamber (**Figure S6c**). The tensile specimen was machined from the rolled sheets along the rolling direction into a flat dumbbell shape with gauge length of 6 mm, width of 2 mm and thickness of 0.8

mm (**Figure S6c**). The sample was loaded with the displacement control at a rate of 0.05 mm/min and then manually stopped at different elongation steps to capture the high-quality SEM images.

ASSOCIATED CONTENT

Supporting Information

Supporting Information is available from the ACS Publications or from the author.

Notes

The authors declare no competing financial interest.

Acknowledgements

The authors want to thank Zijun Ren (Xi'an Jiaotong University Instrument Analysis Center). This work was supported by the National Natural Science Foundation of China (No. 51901192), Shaanxi Science Foundation For Distinguished Young Scholars (2020JC-50), Key Research and Development Projects of Shaanxi Province (No. 2019GY-164, 2021GY-214, 2021SF-296), Science and Technology Project of Weiyang District of Xi'an City (No. 201857, No. 202008), Shaanxi Youth Star Program of Science and Technology (No. 2020KJXX-061), as well as an International Exchange Grant (IEC/NSFC/201078), through the Royal Society, UK and the National Natural Science Foundation of China.

References

[1] Yang, K. M.; Ma, Y. C.; Zhang, Z. Y.;Zhu, J., Sun, Z. B.; Chen, J. S.; Zhao, H. H.; Song, J.; Li, Q.; Chen, N. Q.; Ma, H. Y.; Zhou, J.; Liu, Y.; Fan, T. X. Anisotropic thermal conductivity and associated heat transport mechanism in roll-to-roll graphene reinforced copper matrix composites. *Acta Mater.* **2020**, 197, 342–352.

[2] Han, T. L.; Li, J. J.; Zhao, N. Q.; He, C. N. Microstructure and properties of copper coated graphene nanoplates reinforced Al matrix composites developed by low temperature ball milling. *Carbon* **2020**, 159, 311–323.

[3] Ju, B. Y.; Yang, W. S.; Shao, P. Z.; Hussain, M.; Zhang, Q.; Xiu, Z. Y.; Hou, X. W.; Qiao, J.; Wu, G. H. Effect of interfacial microstructure on the mechanical properties of GNPs/Al composites. *Carbon* **2020**, 162, 346–355.

[4] Li, S. F.; Yang, Y. F.; Misra, R. D. K.; Liu, Y.; Ye, D.; Hu, C. Q.; Xiang, M. Q. Interfacial/intragranular reinforcement of titanium-matrix composites produced by a novel process involving core-shell structured powder. *Carbon* **2020**, 164, 378–390.

[5] Ye, J. L.; Chen, X. H.; Li, J. B.; Liu, C. Q.; Wu, B.; Pan, F. S. Microstructure and compressive properties of Mg–9Al composite reinforced with Ni–coated graphene nanosheets. *Vacuum* **2020**, 181, 109629.

[6] Liu, J.; Wu, M. X.; Yang, Y.; Yang, G.; Yan, H. X.; Jiang, K. Preparation and mechanical performance of graphene platelet reinforced titanium nanocomposites for high temperature applications. *J. Alloy. Compd.* **2018**, 765, 1111–1118.

[7] Huang, L. J.; An, Q.; Geng, L.; Wang, S.; Jiang, S.; Cui, X. P.; Zhang, R.; Sun, F. B.; Jiao, Y.; Chen, X.; Wang, C. Y. Multiscale architecture and superior high-temperature performance of discontinuously reinforced titanium matrix composites. *Adv. Mater.* **2021**, 33, 2000688.

[8] Wang, C. C.; Li, Z. P.; Zhao, H.; Zhang, G. Q.; Ren, T. H.; Zhang, Y. D. Enhanced anticorrosion and antiwear properties of Ti–6Al–4V alloys with laser texture and graphene oxide coatings. *Tribol. Int.* **2020**, 152, 106475.

[9] Mu, X. N.; Cai, H. N.; Zhang, H. M.; Fan, Q. B.; Zhang, Z. H.; Wu, Y.; Ge, Y. X.; Wang, D. D. Interface evolution and superior tensile properties of multi-layer graphene reinforced pure Ti matrix composite. *Mater. Des.* **2018**, 140, 431–441.

[10] Shang, C. Y.; Zhang, F. M.; Zhang, B.; Chen, F. Interface microstructure and strengthening mechanisms of multilayer graphene reinforced titanium alloy matrix nanocomposites with network architectures. *Mater. Des.* **2020**, 196, 109119.

[11] Wu, Y.; Zhang, H. M.; Cai, H. N.; Fan, Q. B.; Mu, X. N. Effects of hot-rolling reduction on microstructure and mechanical properties of GNPs/Ti composites. *Rare Metal Mat. Eng.* **2018**, 47, 2312–2317.

[12] Sadeghi, N.; Aghajani, H.; Akbarpour, M. R. Microstructure and tribological properties of *in-situ* TiC-C/Cu nanocomposites synthesized using different carbon sources (graphite, carbon nanotube and graphene) in the Cu-Ti-C system. *Ceram. Int.* **2018**, 44, 22059–22067.

[13] Dong, L. L.; Xiao, B.; Liu, Y.; Li, Y. L.; Fu, Y. Q.; Zhao, Y. Q.; Zhang, Y. S. Sintering effect on microstructural evolution and mechanical properties of spark plasma sintered Ti matrix composites reinforced by reduced graphene oxides. *Ceram. Int.* **2018**, 44, 17835–17844.

[14] Li, W.; Li, M.; Liu, J.; Yang, Y.; Wen, S. F.; Wei, Q. S.; Yan, C. Z.; Shi, Y. S. Microstructure control and compressive properties of selective laser melted Ti-43.5Al-6.5Nb-2Cr-0.5B alloy: Influence of reduced graphene oxide reinforcement. *Mat. Sci. Eng. A* **2019**, 743, 217–222.

[15] Zhang, X. J.; Song, F.; Wei, Z. P.; Yang, W. C.; Dai, Z. K. Microstructural and mechanical characterization of *in-situ* TiC/Ti titanium matrix composites fabricated by graphene/Ti sintering reaction. *Mat. Sci. Eng. A* **2017**, 705, 153–159.

[16] Guo, S. Y.; Zhang, X.; Shi, C. S.; Liu, E. Z.; He, C. N.; He, F.; Zhao, N. Q. Enhanced mechanical properties and electrical conductivity of graphene nanoplatelets/Cu composites by in situ formation of Mo2C nanoparticles. *Mat. Sci. Eng. A* **2019**, 766, 138365.

[17] Luo, H. B.; Sui, Y. W.; Qi, J. Q.; Meng, Q. K.; Wei, F. X.; He, Y. Z. Mechanical enhancement of copper matrix composites with homogeneously dispersed grapheme modified by silver nanoparticles. *J. Alloy. Comp.* **2017**, 729, 293–302.

[18] Chu, K.; Wang, F.; Li, Y. B.; Wang, X. H.; Huang, D. J.; Geng, Z. R. Interface and mechanical/thermal properties of graphene/copper composite with Mo_2C nanoparticles grown on grapheme. *Compos. Part A* **2018**, 109, 267–279.

[19] Guan, R.; Wang, Y.; Zheng, S.; Su, N.; Ji, Z.; Liu, Z.; An, Y.; Chen, B. Fabrication of aluminum matrix composites reinforced with Ni-coated graphene nanosheets. *Mat. Sci. Eng. A* **2019**, 754, 437–446.

[20] Dong, L. L.; Ding, Y. C.; Huo, W. T.; Zhang, W.; Lu, J. W.; Jin, L. H.; Zhao, Y. Q.; Wu, G. H.; Zhang, Y. S. A green and facile synthesis for rGO/Ag nanocomposites using one-step chemical co-reduction route at ambient temperature and combined first principles theoretical analyze, *Ultrason. Sonochem.* **2019**, 53, 152–163.

[21] Xue, Y. L.; Chen, W. G.; Wang, J. J.; Dong, L. L.; Zhao, Q.; Fu, Y. Q. Formation mechanism and cohesive energy analysis of metal-coated graphene nanocomposites using *in-situ* co-reduction method. *Materials* **2018**, 11, 2071.

[22] Khorshid, M. T.; Kumar, A.; Omrani, E.; Kim, C.; Rohatgi, P. Synthesis, characterization, and properties of graphene reinforced metal-matrix nanocomposites. *Compos. Part B* **2020**, 183, 107664.

[23] Bisht, A.; Srivastava, M.; Kumar, R. M.; Lahiri, I.; Lahiri, D. Strengthening mechanism in graphene nanoplatelets reinforced aluminum composite fabricated through spark plasma sintering. *Mat. Sci. Eng. A* **2017**, 695, 20–28.

[24] Chen, B.; Shen, J.; Ye, X.; Imai, H.; Umeda, J.; Takahashi, M.; Kondoh, K. Solid-state interfacial reaction and load transfer efficiency in carbon nanotubes (CNTs)-reinforced aluminum matrix composites. *Carbon* **2017**, 114, 198–208.

[25] Dong, L. L.; Fu, Y. Q.; Liu, Y.; Lu, J. W.; Zhang, W.; Huo, W. T.; Jin, L. H.; Zhang, Y. S. Interface engineering of graphene/copper matrix composites decorated with tungsten carbide for enhanced physico-mechanical properties. *Carbon* **2021**, 173, 41–53.

[26] Vasanthakumar, K.; Karthiselva, N. S.; Chawake, N. M.; Baksh, S. R. Formation of TiC_x during reactive spark plasma sintering of mechanically milled Ti/carbon nanotube mixtures. *J. Alloy. Compd.* **2017**, 709, 829–841.

[27] Johansson, G. H.; Linde, J. O. Röntgenographische and elektrische Untersuchungen des CuAu-system. *Annalen der physic, Leipzig* **1936**, 5, 1–48.

[28] Yuan, Y.; Liu, Z. G.; Liu, H. W.; Zhao, X. N.; Meng, X. K. The precipitation reaction in a Ag-modified TiAl based intermetallic, as studied by TEM. *J. Alloy. Compd.* **2005**, 399, 126–131.

[29] Liu, B. X.; Huang, L. J.; Wang, B.; Geng, L. Effect of pure Ti thickness on the tensile behavior of laminated Ti–TiB_w/Ti composites. *Mat. Sci. Eng. A* **2014**, 617, 115–120.

[30] Huang, L. J.; Wang, S.; Geng, L.; Kaveendran, B.; Peng, H. X. Low volume fraction in situ (Ti_5Si_3+Ti_2C)/Ti hybrid composites with network microstructure fabricated by reaction hot

pressing of Ti–SiC system. *Compos. Sci. Technol.* **2013**, 82, 23–28.

[31] Liu, B. X.; Huang, L. J.; Geng, L.; Wang, B.; Liu, C.; Zhang, W. C. Fabrication and superior ductility of laminated Ti–TiB_w/Ti composites by diffusion welding. *J. Alloy. Compd.* **2014**, 602, 187–192.

[32] Geng, L.; Ni, D. R.; Zhang, J.; Zheng, Z. Z. Hybrid effect of TiB_w and TiC_p on tensile properties of in situ titanium matrix composites. *J. Alloy. Compd.* **2008**, 463, 488–92.

[33] Ma, F. C.; Zhou, J. J.; Liu, P.; Li, W.; Liu, X. K.; Pan, D.; Lu, W. J.; Zhang, D.; Wu, L. Z.; Wei, X. Q. Strengthening effects of TiC particles and microstructure refinement in *in situ* TiC-reinforced Ti matrix composites. *Mater. Charact.* **2017**, 127, 27–34.

[34] Mu, X. N.; Zhang, H. M.; Cai, H. N.; Fan, Q. B.; Zhang, Z. H.; Wu, Y.; Fu, Z. J.; Yu, D. H. Microstructure evolution and superior tensile properties of low content graphene nanoplatelets reinforced pure Ti matrix composites. *Mat. Sci. Eng. A* **2017**, 687, 164–174.

[35] Li, S. F.; Sun, B.; Imai, H.; Kondoh, K. Powder metallurgy Ti–TiC metal matrix composites prepared by in situ reactive processing of Ti-VGCFs system. *Carbon* **2013**, 61, 216–228.

[36] Mu, X. N.; Cai, H. N.; Zhang, H. M.; Fan, Q. B.; Wang, F. C.; Zhang, Z. H.; Ge, Y. X.; Shi, R.; Wu, Y.; Wang, Z.; Wang, D. D.; Chang, S. Uniform dispersion and interface analysis of nickel coated graphene nanoflakes/pure titanium matrix composites. *Carbon* **2018**, 137, 146–155.

[37] Kondoh, K.; Threrujirapapong, T.; Imai, H.; Umeda, J.; Fugetsu, B. Characteristics of powder metallurgy pure titanium matrix composite reinforced with multi-wall carbon nanotubes. *Compos. Sci. Technol.* **2009**, 69, 1077–1081.

[38] Zhang, F. M.; Liu, T. F. Nanodiamonds reinforced titanium matrix nanocomposites with network architecture. *Compos. Part B* **2019**, 165, 143–154.

[39] Dong, L. L.; Xiao, B.; Jin, L. H.; Lu, J. W.; Liu, Y.; Fu, Y. Q.; Zhao, Y. Q.; Wu, G. H.; Zhang, Y. S. Mechanisms of simultaneously enhanced strength and ductility of titanium matrix composites reinforced with nanosheets of graphene oxides. *Ceram. Int.* **2019**, 45, 19370–19379.

[40] Yang, Z. F.; Lu, W. J.; Zhao, L.; Qin, J. N.; Zhang, D. Microstructure and mechanical property of in situ synthesized multiple-reinforced (TiB+TiC+La_2O_3)/Ti composites. *J. Alloy. Compd.* **2008**, 455, 210–214.

[41] Liu, Y.; Dong, L. L.; Lu, J. W.; Huo, W. T.; Du, Y.; Zhang, W.; Zhang, Y. S. Microstructure and mechanical properties of SiC nanowires reinforced titanium matrix composites. *J. Alloy.*

Compd. **2020**, 819, 152953.

[42] Wei, S.; Zhang, Z. H.; Wang, F. C.; Shen, X. B.; Cai, H. N.; Lee, S. K.; Wang, L. Effect of Ti content and sintering temperature on the microstructures and mechanical properties of TiB reinforced titanium composites synthesized by SPS process. *Mat. Sci. Eng. A* **2013**, 560, 249–255.

[43] Feng, H. B.; Zhou, Y.; Jia, D. C.; Meng, Q. C. Microstructure and mechanical properties of in situ TiB reinforced titanium matrix composites based on Ti–Fe-Mo–B prepared by spark plasma sintering. *Compos. Sci. Technol.* **2004**, 64, 2495–2500.

[44] Zhang, Z. H.; Shen, X. B.; Wen, S.; Luo, J.; Lee, S. K.; Wang, F. C. *In situ* reaction synthesis of Ti–TiB composites containing high volume fraction of TiB by spark plasma sintering process. *J. Alloy. Compd.* **2010**, 503, 145–150.

[45] Degnah, A.; Du, J.; Ravi, K. S. Chandran CALPHAD Approach and processing of a multicomponent titanium matrix composite for high strength and fracture toughness. *Mat. Sci. Eng. A* **2020**, 781, 139210.

[46] Ji, X.; Zhang, C. J.; Sun, Y. G.; Zhang, S. Z.; Feng, H.; Han, F. Y.; Chen, Y. Y. Microstructure and mechanical properties of TiC/Ti composites with different carbon sources. *Titanium Ind. Prog.* **2020**, 37, 23–28.

[47] Yang, J. H.; Xiao, S. L.; Chen, Y. Y.; Xu, L. J.; Wang, X. P.; Zhang, D. D. The tensile and fracture toughness properties of a (TiB_w + TiC_p)/Ti-3.5Al-5Mo-6V-3Cr-2Sn-0.5Fe composites after heat treatment. *Mat. Sci. Eng. A* **2018**, 729, 21–28.

[48] Tan, Y. D.; Xu, L. Y.; Xu, Z. Q.; Ali, T.; Ma, Z. L.; Cheng, X. W.; Cai, H. N. Effects of Ti foil thickness on microstructures and mechanical properties of in situ synthesized micro-laminated TiC/Ti composites. *Mat. Sci. Eng. A* **2019**, 767, 138296.

[49] Oh, J. C.; Lee, S. Correlation of microstructure with hardness and fracture properties of (TiC, SiC)/Ti-6Al-4V surface composites fabricated by high-energy electron-beam irradiation. *Surf. Coat. Tech.* **2004**, 179, 340–348.

[50] Selvakumara, M.; Chandrasekar, P.; Mohanraj, M.; Ravisankar, B.; Balaraju, J.N. Role of powder metallurgical processing and TiB reinforcement on mechanical response of Ti–TiB composites. *Mater. Lett.* **2015**, 144, 58–61.

[51] Chu, K.; Wang, J.; Liu, Y. P.; Geng, Z. R. Graphene defect engineering for optimizing the interface and mechanical properties of graphene/copper composites. *Carbon* **2018**, 140, 112–123.

[52] Tsai, P. C.; Jeng, Y. R. Experimental and numerical investigation into the effect of carbon nanotube buckling on the reinforcement of CNT/Cu composites. *Compos. Sci. Technol.* **2013**, 79, 28–34.

[53] Dong, H. N.; Seung, I. C.; Byung, K. L.; Hoon, M. P.; Do S. H., Soon, H. H. Synergistic strengthening by load transfer mechanism and grain refinement of CNT/Al–Cu composites. *Carbon* **2012**, 50, 2417–2423.

[54] Munir, K. S.; Zheng, Y. F.; Zhang, D. L.; Lin, J. X.; Li, Y. C.; Wen, C. Microstructure and mechanical properties of carbon nanotubes reinforced titanium matrix composites fabricated via spark plasma sintering. *Mat. Sci. Eng. A* **2017**, 688, 505–523.

[55] Wei, L. X.; Liu, X. Y.; Gao, Y. Z.; Lv, X. W.; Hu, N.; Chen, M. Synergistic strengthening effect of titanium matrix composites reinforced by graphene oxide and carbon nanotubes. *Mater. Des.* **2021**, 197, 109261.

[56] Su, Y. S.; Li, Z.; Yu, Y.; Zhao, L.; Li, Z. Q.; Guo, Q.; Xiong, D. B.; Zhang, D. Composite structural modeling and tensile mechanical behavior of graphene reinforced metal matrix composites. *Sci. China Mater.* **2018**, 61, 112–124.

[57] Liu, X. H.; Li, J. J.; Sha, J. W.; Liu, E. Z.; Li, Q. Y.; He, C. N.; Shi, C. S.; Zhao, N. Q. *In-situ* synthesis of graphene nanosheets coated copper for preparing reinforced aluminum matrix composites. *Mat. Sci. Eng. A* **2018**, 709, 65–71.

[58] Dong, L. L.; Lu, J. W.; Fu, Y. Q.; Huo, W. T.; Liu, Y.; Li, D. D.; Zhang, Y. S. Carbonaceous nanomaterial reinforced Ti-6Al-4V matrix composites: Properties, interfacial structures and strengthening mechanisms. *Carbon* **2020**, 164, 272–286.

[59] Chen, B.; Li, S. F.; Imai, H.; Umeda, J.; Takahashi, M.; Kondoh, K. Inter-wall bridging induced peeling of multi-walled carbon nanotubes during tensile failure in aluminum matrix composites. *Micron* **2015**, 69, 1–5.

[60] Taguchi, O.; Iijima, Y. Diffusion of copper, silver and gold in α-titanium. *Philos. Mag. A* **1995**, 72, 1649–1655.

[61] Dong, L. L.; Chen, W. G.; Deng, N.; Zheng, C. H. A novel fabrication of graphene by chemical reaction with a green reductant. *Chem. Eng. J.* **2016**, 306, 754–762.

[62] Perdikaki, A.; Galeou, A.; Pilatos, G.; Karatasios, I.; Kanellopoulos, N. K.; Prombona, A.; Karanikolos, G. N. Ag and Cu monometallic and Ag/Cu bimetallic nanoparticle – graphene

composites with enhanced antibacterial performance. *ACS Appl. Mater. Inter.* **2016**, 8, 27498–27510.

[63] Chen, Y. C.; Zhang, X.; Liu, E. Z.; He, C. N.; Shi, C. S.; Li, J. J.; Nash, P.; Zhao, N. Q. Fabrication of *in-situ* grown graphene reinforced Cu matrix composites. *Sci. Rep.* **2016**, 6, 19363.

[64] Tourino, I. L.; Naranjo, A. C.; Arce, M. P. A molecular dynamics modelling adsorption study of Cu and Ag nanoparticles on pristine and functionalized graphene surfaces. *Mater. Today: Process.* **2020**, 33, 1830–1834.

[65] Kikuchi, M.; Takada, Y.; Kiyosue, S.; Yoda, M.; Woldu, M.; Cai, Z.; Okuno, O.; Okabe, T. Mechanical properties and microstructures of cast Ti-Cu alloys. *Dent. Mater.* **2003**, 19, 174–181.

[66] Han, M. K.; Hwang, M. J.; Won, D. H.; Kim, Y. S.; Song, H. J.; Park, Y. J. Massive transformation in titanium-silver alloys and its effect on their mechanical properties and corrosion behavior. *Materials* **2014**, 7, 6194–6206.

[67] Tian, N.; Dong, L. L.; Wang, H. L.; Fu, Y. Q.; Huo, W. T.; Liu, Y.; Yu, J. S.; Zhang, Y. S. Microstructure and tribological properties of titanium matrix nanocomposites through powder metallurgy using graphene oxide nanosheets enhanced copper powders and spark plasma sintering. *J. Alloy. Compd.* **2021**, 867, 159093.

[68] Bao, M. M.; Liu, Y.; Wang, X. Y.; Yang, L.; Li, S. Y.; Ren, J.; Qin, G. W.; Zhang, E. L. Optimization of mechanical properties, biocorrosion properties and antibacterial properties of wrought Ti-3Cu alloy by heat treatment. *Bioact. Mater.* **2018**, 3, 28–38.

[69] H. Gietl, H.; Olbrich, S.; Riesch, J.; Holzner, G.; Höschen, T.; Coenen, J.W.; Neu, R. Estimation of the fracture toughness of tungsten fibre-reinforced tungsten composites. *Eng. Fract. Mech.* **2020**, 232, 107011.